Physically Based Model for Multispectral Image Simulation of Earth Observation Sensors

Xiaoyu He and Xiaojian Xu

***Abstract*—Physically based multispectral image simulation consists of sensor system modeling, bottom-of-atmosphere (BOA) image generation, and top-of-atmosphere (TOA) image calculation. TOA radiance images are usually generated using a lookup table (LUT) for computational efficiency, which is calculated by means of atmospheric radiative transfer codes with different combination of input variables, including viewing zenith, solar zenith, and relative azimuth angles; visibility; columnar water vapor; and ground elevation. In this paper, a new strategy is proposed for TOA radiance image simulation, where transmitted surface radiance and atmospheric radiance at the TOA are calculated, respectively, to improve accuracy as well as efficiency. The transmitted surface radiance image is obtained from pixel-by-pixel calculation of BOA radiance and path transmittance. In calculating the atmospheric radiance of TOA, two LUTs are built for the emitted and the scattered radiance from each atmospheric layer, respectively. The effects of visibility and columnar water vapor on the atmospheric radiance are characterized by means of an equivalent path transmittance, which is related to the scene geometry as well as the thickness of atmospheric layer. In this way, when a new scene is simulated, except for three variables, i.e., viewing and solar zenith angles and atmospheric layer number, other parameters are set as constants in building the LUTs, enabling more combinations of input variables without adding excessive computational burden. Multispectral images in different bands with moderate spatial resolution are simulated and compared with the moderate-resolution imaging spectroradiometer (MODIS) images to demonstrate the accuracy and the usefulness of the proposed strategy.**

***Index Terms*—Earth observation sensor, infrared image simulation, multispectral image, physically based model, radiative transfer calculation.**

I. Introduction

GLOBAL remote sensing gains importance in an adversity of applications in environmental management and security. With the improvement of spectral resolution, multispectral and hyperspectral spaceborne sensors [1]–[4] can provide high-resolution data about the spectral characteristics of the Earth for scientific studies [5], [6] as well as practical applications [7], [8].

Physically based image simulation is an effective tool in infrared (IR) sensor design. A number of end-to-end simulation models were developed covering different spectral ranges for various remote sensing missions. Examples include the Environmental Mapping and Analysis Program (EnMAP) end-to-end Simulation (EeteS) software [9], the Sentinel-2 end-to-end Simulation (S2eteS) software [10], Land Scene Generator (LSG) [11] for the Sentinel-3 mission [4], the Software ENviroment for the Simulation of Optical Remote sensing systems (SENSOR) [12] for the Airborne Prism EXperiment (APEX) [13], simulator for the Surface Processes and Ecosystem Change Through Response Analysis (SPECTRA) mission [14], performance simulator for the FLuorescence EXplorer (FLEX) mission [15], and the simulation and analytical model of the Compact Reconnaissance Imaging Spectrometer for Mars (CRISM) [16]. Other simulation approaches were also proposed for scientific studies. Examples are the Digital Imaging and Remote Sensing Image Generation (DIRSIG) model [17], the Parameterized Image Chain Analysis and Simulation SOftware (PICASSO) [18], the Discrete Anisotropic Radiative Transfer (DART) [19], and simulation of top-of-atmosphere (TOA) image in 4.3 μm band [20]. The simulated images can be used for developing and testing algorithms in fields, including band selection [21], image segmentation [22], atmospheric compensation [23], land-cover discrimination [24], and spectral unmixing [25].

In general, remote sensing images can be simulated following three steps, i.e., generating bottom-of-atmosphere (BOA) images, calculating atmospheric effects on TOA radiance, and modeling IR sensor system to generate synthetic images. The BOA images, including the Earth surface reflection and emission images are usually generated using spectral and spatial interpolations and extrapolations to adjust existing remote sensing images. The approach has been validated in transmittance spectral bands [9]–[12], [18]. When the BOA images are obtained, atmospheric transfer codes are utilized to calculate TOA radiance images. The pixel-by-pixel calculation of TOA radiance is adopted to simulate the images covering small ground areas [14], [19]. However, to improve computational efficiency for simulating images covering thousands of kilometers, the TOA radiance images are generated using a lookup table (LUT) calculated by means of the atmospheric transfer codes with different combination of input variables [11], [20], [26], [27]. The calculated TOA images are used as the input of IR sensor system models to generate synthetic images in different spectral bands [9]–[16].

In the previous simulation [20], [26], [27], a comprehensive LUT with six variables is built to improve efficiency of the TOA radiance calculation. The combinations of input variables (defined as breakpoints in [26]) are selected elaborately to

Manuscript received September 17, 2016; revised December 20, 2016; accepted January 17, 2017. Date of publication February 13, 2017; date of current version April 10, 2017. *(Corresponding author: Xiaoyu He.)*

The authors are with the School of Electronics and Information Engineering, Beihang University, Beijing, 100083, China (e-mail: hexiaoyu@buaa.edu.cn; xiaojianxu@buaa.edu.cn).

Color versions of one or more of the figures in this paper are available online at http://ieeexplore.ieee.org.

Digital Object Identifier 10.1109/JSTARS.2017.2658678

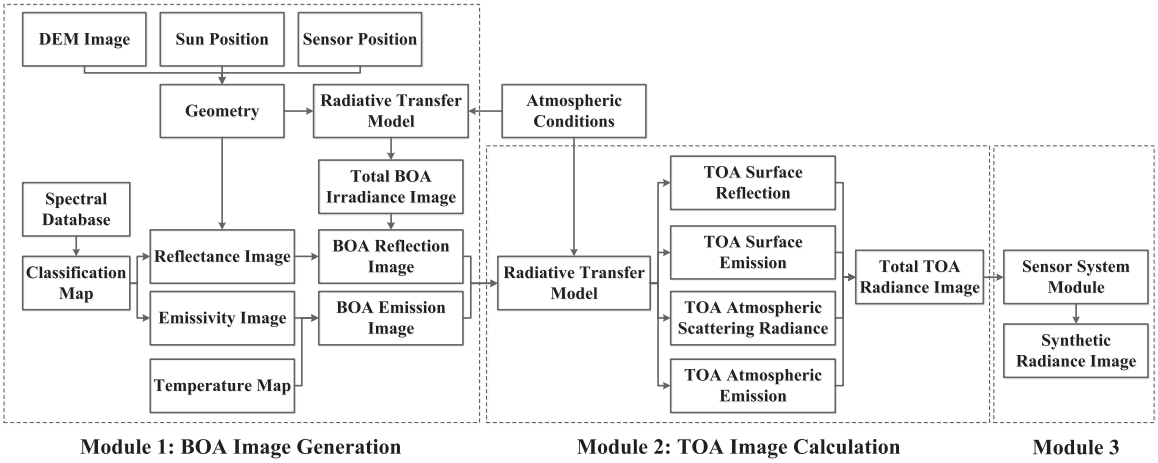

Fig. 1. Flowchart of radiance image simulation for Earth observation sensors.

compromise sufficient sampling and the LUT size since a few extra samples of one variable will lead to a dramatic increase of computational time and storage capacity. As a result, the TOA radiance calculated with extreme variable values are not included in the LUT. Examples are viewing zenith angle close to 90° (the Earth limb observation) and visibility lower than 10 km. Besides, the available BOA images depend upon the coverage area and the observational bands of existing satellite images.

The aim of this paper is to develop a physically based image simulation model for Earth observation sensors which allows multispectral image simulation from visible to thermal IR bands. In the simulation of TOA radiance image, based on the assumption that the Earth is an ideal sphere with constant temperature, a procedure was earlier presented by the authors [28]. As an extension, a new strategy is proposed for TOA radiance image simulation in this paper, where transmitted surface radiance and atmospheric radiance at the TOA are calculated, respectively, to improve accuracy of simulation as well as its efficiency. The transmitted surface radiance image is obtained from pixel-by-pixel calculation of BOA radiance and path transmittance. To calculate the atmospheric radiance of TOA efficiently, two LUTs are built for the emitted and the scattered radiance from each atmospheric layer, respectively, where a few approximations are adopted to reduce necessary variables. The LUTs are built with three variables enabling more breakpoints without adding excessive computational burden. To generate BOA images for various scenes under different illumination and observation geometries, the pixel-by-pixel variation of spatial information on the Earth surface, namely image texture, is obtained by means of consulting a prebuilt database. The database is established at a spatial resolution of 1 arc minute with public data, including a global land cover feature map [29], material spectral characteristic data [30]–[32], a digital elevation model (DEM) [33], and global surface temperature maps [34]–[36]. Since the spatial resolution of the BOA images is limited to the collected data, the current model is suitable to generate satellite images at a moderate spatial resolution, such as images for the moderate-resolution imaging spectroradiometer (MODIS) [37] and the Visible Infrared Imaging Radiometer Suite (VIIRS) [38]. The sensor system is modeled using the methods introduced in [39] and [40].

The remainder of this paper is organized as follows. Section II makes a brief introduction to the model framework including database preparation, geometry calculation, and surface texture generation. The strategy for TOA image calculation is detailed in Section III, where the LUTs are built in a different way to improve accuracy as well as efficiency. In Section IV, simulation examples are presented to demonstrate the accuracy and the usefulness of the proposed strategy. We conclude the paper in Section V.

II. Model Framework

The procedure for radiance image simulation is descripted in Fig. 1. As it can be seen, the model consists of BOA image generation, TOA image calculation, and sensor system modules. Only the modules of the BOA image generation and the TOA image calculation are introduced in this paper since the sensor system module has been detailed in [39] and [40]. The approach for BOA image generation is described in the following while the strategy for TOA radiance calculation will be discussed in the next section.

As it can be seen in Fig. 1, BOA images, including the reflection and the emission images are obtained in module 1. To generate surface texture, based on the assumption that the Earth terrain changes over time slowly, a comprehensive database of the Earth surface is built integrating different public data sets. The surface texture images can be generated via consulting the database with latitude and longitude images. Since the spatial resolutions of most available data are 1 arc minute (geographic projection), the surface texture images can only be generated at a moderate spatial resolution. Scarce global surface feature data at a high spatial resolution can be a bottleneck of the current model.

A. Reflection Image

The BOA reflection can be calculated as

$$E_r(\lambda,\ \theta_v,\ \theta_s,\ \phi) = E_d(\lambda,\ \theta_v,\ \theta_s,\ \phi) \cdot \rho_r(\lambda,\ \theta_v,\ \theta_s,\ \phi) \tag{1}$$

where E_r is the BOA spectral reflection, E_d is the spectral irradiance at the BOA, ρ_r is the reflectance of a surface illuminated from a direction (θ_s, ϕ_s) and observed from a direction (θ_v, ϕ_v), λ is the wavelength, θ_v is the viewing zenith angle, θ_s is the solar zenith angle, and ϕ is the relative azimuth angle between the solar and the viewing geometries.

In most simulation models [9]–[12], BOA reflection image is generated using interpolation and extrapolation to adjust existing satellite images. However, the BOA reflection in (1) is calculated with the BOA irradiance and the reflectance. As shown in Fig. 1, the BOA irradiance E_d is obtained from atmospheric radiative transfer model, which will be detailed in the Section III.

The bidirectional reflectance distribution function (BRDF) proposed by Rahman *et al*. [41] is adopted to calculate the reflectivity varying with illumination and observation geometries. In flat terrain, the reflectance ρ_r can be expressed as

$$\rho_r(\lambda,\ \theta_v,\ \theta_s,\ \phi) = \rho_g(\lambda)\frac{\cos^{a-1}\theta_v \cos^{a-1}\theta_s}{(\cos\theta_v + \cos\theta_s)^{1-a}} F(\phi)[1 + R(G)] \tag{2}$$

where ρ_g is the surface spectral reflectivity, a is the empirical structural parameter indicating the surface anisotropy level, *F* is the modified Henyey & Greenstein's function, *R* is the function accounting for hot spot effect, and *G* is the geometric factor.

When topographic effect is considered, the solar and the viewing zenith angles in (2) are substituted by the solar incident angle and the viewing angle, respectively. The solar incident angle, a key factor in BRDF, depends upon the solar zenith and the azimuth angles as well as terrain slope and aspect derived from DEM [42], [43].

The ETOPO1 elevation map [33], a global relief model with 1 arc minute spatial resolution at a height accuracy of 1 m is utilized as the DEM in modeling. At an arbitrary acquisition time, the viewing zenith and azimuth angles depend upon the position of the sensor while the solar zenith and azimuth angles depend upon the position of the sun. Z-buffer algorithm [44] is adopted to calculate the geometry variables for each pixel, including surface elevation, the viewing angle, the solar incident angle, and the relative azimuth angle. In this way, a surface bidirectional reflectance image involving topographic effect can be obtained via substituting the calculated geometry variables into (2).

Besides, the surface elevation is related to atmospheric path transmittance due to the fact that atmospheric density varies with altitude.

The surface spectral reflectivity ρ_g, another important factor in BRDF, is different for each type of land cover. The land cover classification map of the International Geosphere Biosphere Programme (IGBP) [45] is used in the model where the Earth surface is classified into 17 different types. The IGBP map with geographic projection at a spatial resolution of 0.5 arc minute is available on the U.S. Geological Survey (USGS) website [29].

The reflectivity and emissivity profiles of various materials are provided by different spectral databases [30]–[32]. These data are interpolated into 1 nm spectral resolution covering wavelength range from 0.4 to 14.5 μm. For a classification map with moderate spatial resolution, a single type of land cover usually consists of several different materials leading to a mixing spectral characteristic. The mixing coefficients for the IGBP map are given subjectively with reference to linear combinations in [46] and [47], as listed in Table I.

TABLE I
ASSIGNMENTS OF MATERIAL SPECTRAL PROFILES TO SURFACE TYPES

ID	Surface Type	Material	Mixing Ratio
1	Evergreen Needle leaf Forest	Spruce, pine	1:1
2	Evergreen Broad leaf Forest	Laurel, Sycamore	1:1
3	Deciduous Needle leaf Forest	Ponderosa, Magnolia, Hawthorne	1:1:1
4	Deciduous Broad leaf Forest	Oak, Maple	1:1
5	Mixed Forest	ID1-ID4	1:1:1:1
6	Closed Shrub lands	Sagebrush, Quartz Sand	3:1
7	Open Shrub lands	Sagebrush, Quartz Sand	1:3
8	Woody Savannas	Grassland, ID1, ID2	6:1:1
9	Savannas	Grassland, ID1, ID2	18:1:1
10	Grassland	Grassland	1
11	Permanent Wetlands	Grassland, Seawater	1:1
12	Croplands	Bean	1
13	Urban and Built-Up	Grassland, ID5, Concrete	5:4:1
14	Natural Vegetation Mosaic	ID5, ID12	1:1
15	Snow and Ice	Fresh snow, Old snow	1:1
16	Barren or Sparsely Vegetated	Quartz Sand	1
17	Water Bodies	Seawater	1

B. Emission Image

The BOA emission can be expressed as

$$E_g(\lambda) = \varepsilon_g(\lambda) \cdot B(\lambda, T_g) \tag{3}$$

where E_g is the BOA spectral emission, *B* is the Planck function, T_g is the surface temperature, and ε_g is the spectral emissivity calculated by the spectral reflectivity with Kirchhoff's law, which can be written as

$$\varepsilon_g(\lambda) = 1 - \rho_g(\lambda). \tag{4}$$

It is a challenge to predict surface emission precisely since the surface temperature is changing every day, even every hour. For simplification of the problem, monthly average temperature maps are included in the current model to study the spectral emission characteristics of the Earth surface.

Three public databases are integrated to build monthly average temperature maps at a spatial resolution of 1 arc minute. The land temperature maps at a spatial resolution of 0.5 arc minutes are provided by the WorldClim website [34]. The ocean temperature maps obtained from the MODIS are available on the NASA's website with a spatial resolution of 6 arc minutes [35]. The global surface temperature maps at a spatial resolution of 60 arc minutes offered by the Berkeley Earth [36] are utilized as supplementary data to fill the blank pixels.

III. TOA IMAGE CALCULATION

TOA radiance consists of transmitted surface radiance and atmospheric radiance. Since path transmittance can be calculated efficiently using transfer path length and extinction coefficient, the transmitted surface radiance image is obtained from pixel-by-pixel calculation to ensure accuracy. On the other hand, LUTs

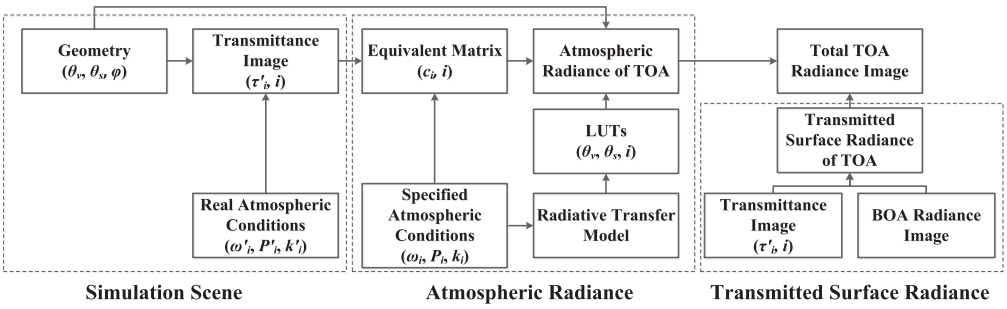

Fig. 2. Procedure of calculating TOA radiance image. Two blocks of transmittance image are the same.

are built for the atmospheric radiance to improve computational efficiency. The procedure of TOA image calculation with the equivalent coefficient is described in Fig. 2.

In previous LUTs, the input parameters of atmospheric radiative transfer model [48]–[50] are utilized as variables, which include atmospheric model; aerosol type; viewing zenith, solar zenith, and relative azimuth angles; surface elevation; visibility; and columnar water vapor. The LUTs with six to eight variables have a disadvantage in setting breakpoints since a few extra samples of one variable will lead to a dramatic increase of computational time and storage capacity. In the proposed strategy, the parameters in radiative transfer equations are selected as variables to build LUTs in the developed model. Then, a few approximations are taken to reduce necessary variables enabling more breakpoints without adding excessive computational burden. The basic radiative transfer equations are given to detail this idea in the following.

The total TOA radiance E_t consists of four types of radiations and can be written as

$$E_t = E_r + E_b + E_s + E_e \tag{5}$$

where E_r is the surface reflection, E_b is the surface emission, E_s is the atmospheric scattered radiance, and E_e is the atmospheric emission.

Due to the fact that the atmospheric density varies with altitude, the inhomogeneous atmosphere is divided into a number of homogenous layers during radiative transfer calculation. As shown in Fig. 3, assuming the atmosphere consists of *n* layers while the ground with an elevation of *H* is located in the *m*th layer.

To simplify the expression, the wavelength λ is omitted in the following equations. Four types of radiations in (5) can be expressed as

$$E_r(\theta_v,\ \theta_s,\ \phi) = E_0 \cdot \rho_r(\theta_v,\ \theta_s,\ \phi) \cdot \prod_{i=1}^{m} [\tau_i(\theta_v) \cdot \tau_i(\theta_v)] \tag{6}$$

$$E_b(\theta_v) = E_g \cdot \prod_{i=1}^{m} \tau_i(\theta_v) \tag{7}$$

$$E_s(\theta_v,\ \theta_s,\ \varphi) = \sum_{i=1}^{m} [c_i \cdot E_{s-i}(\theta_v,\ \theta_s,\ \varphi)] \tag{8}$$

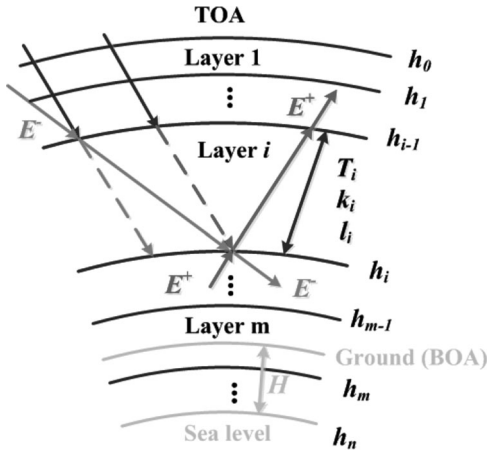

Fig. 3. Sketch of radiative transfer calculation.

$$E_e(\theta_v) = \sum_{i=1}^{m} [c_i \cdot E_{e-i}(\theta_v)] \tag{9}$$

with

$$E_{s-i}(\theta_v,\ \theta_s,\ \varphi) = E_0 \cdot \omega_i \cdot P_i(\varphi) \cdot [1 - \tau_{s-i}(\theta_s) \cdot \tau_{s-i}(\theta_v)] \cdot \prod_{j=1}^{i-1} (\tau_j(\theta_s) \cdot \tau_j(\theta_v)) \tag{10}$$

$$E_{e-i}(\theta_v) = (1 - \omega_i) \cdot [1 - \tau_{s-i}(\theta_v)] \cdot B(T_i) \cdot \prod_{j=1}^{i-1} \tau_j(\theta_v) \tag{11}$$

$$\cos\varphi = \cos\theta_v \cos\theta_s + \sin\theta_v \sin\theta_s \cos\phi \tag{12}$$

where E_{e-i} and E_{s-i} are, respectively, the spectral emission and the spectral scattered radiance of the *i*th layer at the TOA; E_g is the surface spectral emission calculated in (3); E_0 is the solar TOA spectral irradiance; τ_{s-i} and τ_{i} are the spectral transmittances of the direct and the total radiation in the *i*th layer, respectively; ω_i is the spectral albedo in the *i*th layer; T_i is the atmospheric temperature in the *i*th layer; P_i is the phase function in the *i*th layer; φ is the scattering angle; ρ_r is the reflectance computed in (2); and c_i is the equivalent coefficient added manually for approximation, which is equal with one in atmospheric radiative transfer calculation.

The transmittances τ_{s-i} and τ_i are related to atmospheric conditions and transfer path lengths, i.e.

$$\tau_{s-i}(\theta) = \exp(-l_i(\theta) \cdot k_i) \tag{13}$$

$$\tau_i(\theta) = \tau_{s-i}(\theta) + (1 - \tau_{s-i}(\theta)) \cdot \omega_i \cdot P_{0-i} \tag{14}$$

where k_i is the spectral extinction coefficient in the *i*th layer; l_i is the path length in the *i*th layer solved with the zenith angle θ and the thickness of the *i*th layer; and P_{0-i} is the phase function of diffuse radiation in the *i*th layer.

From (5) through (12), the parameters in radiative transfer equations can be classified into two sets. One set is related to geometry, including viewing zenith angle θ_v, solar zenith angle θ_s, and relative azimuth angle ϕ. The other set depends upon atmospheric conditions [51], which includes albedo ω_i, phase function P_i, atmospheric temperature T_i, and extinction coefficient k_i. When one set of atmospheric conditions is specified to calculate TOA radiance, the effects of atmospheric condition variation on the atmospheric radiance of TOA are expected to be approximated using the equivalent coefficient c_i. In this way, except for viewing zenith, solar zenith, and relative azimuth angles, other variables are set as constants in building LUTs.

A. Approximation with Equivalent Coefficient

As shown in Fig. 2, the variables related to real atmospheric conditions are distinguished with a hat while the specified atmospheric conditions are set subjectively.

Similar to (13) and (14), the image of total transmittance in the *i*th layer can be calculated as

$$\hat{\tau}_i(\theta) = \exp(-\hat{l}_i(\theta) \cdot \hat{k}_i) + [1 - \exp(-\hat{l}_i(\theta) \cdot \hat{k}_i)] \cdot \hat{\omega}_i \cdot \hat{P}_{0-i}. \tag{15}$$

Substituting the real atmospheric condition parameters in (15) with the specified parameters, the equivalent transfer path length in the *i*th layer l_i^* can be solved from

$$l_i^* = -\frac{1}{k_i} \ln\left(\frac{\hat{\tau}_i - \omega_i P_{0-i}}{1 - \omega_i P_{0-i}}\right) \tag{16}$$

where $\hat{\tau}_i$ is the estimate of the real transmittance of the *i*th layer calculated in (15) and k_i, ω_i, and P_{0-i} are the parameters related to the specified atmospheric conditions.

It should be noticed that the real atmospheric parameters are usually not completely known in the simulation of wide-swath images. The atmospheric parameters derived from existing sensor images are used to retrieve an estimate of the real transmittance in (15) and (16).

For transfer paths at specific zenith angles, the transfer path lengths in the *i*th layer can be solved with the zenith angles and thickness of the *i*th layer. To simplify expression, the relationship equation under the assumption of plane-parallel atmosphere is given as

$$\Delta h_i = l_i / \cos\theta \tag{17}$$

where $\Delta h_i = h_{i-1} - h_i$ is the thickness of the *i*th layer. As shown in Fig. 3, the thickness of the *m*th layer is obtained from $\Delta h_m = h_{m-1} - H$.

Then, the equivalent coefficient in the *i*th layer can be defined as

$$c_i = \Delta h^*{}_i / \Delta h_i \tag{18}$$

where Δh_i^* is the equivalent thickness of the *i*th layer, which is calculated via replacing l_i with l_i^* in (17). It should be noted that $\Delta h_{\mathrm{i}}{}^*$ can be calculated in incident and viewing paths, respectively. Ideally, the solutions are the same for two paths. A weighted factor is added in case of unexpected differences.

As it can be seen in Fig. 2, only one set of atmospheric conditions is used in building LUTs. Considering the vertical variation of atmospheric conditions, the layer number is added into the LUTs as an extra variable. For geometry variables, since the relative azimuth angle ϕ can be calculated using the viewing zenith angle θ_v and the solar zenith angle θ_s [28] in a specific scene, only θ_v and θ_s are selected as interpolation variables. Then, interpolation is implemented on a two-dimensional (2-D) space to calculate the emitted and the scattered radiance from each atmospheric layer. Since the radiance from upper atmosphere is less intense than that from lower atmosphere, the computational time can be saved via reducing the number of atmospheric layers at higher altitude.

From (15) through (18), the equivalent coefficient matrix characterizes the spatial distribution of atmospheric conditions in a specific scene. Instead of building a comprehensive LUT with all possible variables in the previous method, the LUTs are built for each simulation scene separately in the proposed strategy. The LUTs allow more breakpoints to simulate images with extreme variable values whereas the equivalent coefficient c_{i} will inevitably case extra accuracy loss in the TOA radiance calculation. It should be noted that the vertical profile of atmospheric temperature is assumed the same for all pixels to simplify simulation.

B. Approximation with Average Reflectivity and Emissivity

The approach proposed in Section III-A can be used to calculate spectral radiance at the TOA. For multispectral sensors, the spectral radiance should be integrated in specific bands to generate radiance images. As it can be seen from (6) and (7), the surface reflection and emission are related to the spectral reflectivity and emissivity. For computational efficiency, average reflectivity $\bar{\rho}_g$ and emissivity $\bar{\varepsilon}_g$ are utilized to generate BOA images in specific bands, which are, respectively, defined as

$$\bar{\rho}_g = \sum_{\lambda_1}^{\lambda_2} [\rho_g(\lambda) \cdot E_0(\lambda)] / \sum_{\lambda_1}^{\lambda_2} E_0(\lambda) \tag{19}$$

$$\bar{\varepsilon}_g = \sum_{\lambda_1}^{\lambda_2} [\varepsilon_g(\lambda) \cdot B(\lambda, T_g)] / \sum_{\lambda_1}^{\lambda_2} B(\lambda, T_s) \tag{20}$$

where ρ_g and ε_g are, respectively, the spectral reflectivity and emissivity of surface described in (2) and (3); λ_1 and λ_2 are the cut-in and the cut-off wavelength, respectively; and T_s is the assumed surface temperature.

In this way, the coupling between atmospheric radiative transfer and surface radiance can be obtained from the average

TABLE II
SIMULATION PARAMETERS FOR MODIS IMAGE SIMULATION

	Parameters	Values
Data file information	Date	2015003 (Jan. 3, 2015)
	Hour	5:30 a.m. to 5:35 a.m.
	Bands	Band 6 (1.628−1.652 μm)
		Band 7 (2.105−2.155 μm)
	Image size	2708 × 4080
Sensor	Orbit height	705 km
	FOV	110°×163.2°
	IFOV	0.04°
	Effective pupil diameter	17.78 cm
	Effective focal length	380.86 mm
	Operating temperature of focal plane	293 K
	Calibration accuracy	±2%
Specified atmospheric conditions	Atmospheric model	Mid-latitude winter
	Boundary aerosol type	Rural
	Relative humidity	0.7
	Visibility	18 km
LUTs	Solar zenith angles	51.7°−67.2° in step of 0.1°
	Viewing zenith angles	−65.5° to 65.5° in step of 0.2°
	Atmospheric layers	0−100 km, 60 layers in total

reflectivity and emissivity [49], which can be expressed as

$$\rho_g^* = \frac{\bar{\rho}_g}{1 - \bar{\rho}_g \cdot \bar{\omega}} \tag{21}$$

$$\varepsilon_g^* = \frac{\bar{\varepsilon}_g}{1 - (1 - \bar{\varepsilon}_g) \cdot \bar{\omega}} \tag{22}$$

where ρ_g^* and ε_g^* are, respectively, the total reflectivity and emissivity; and is the total atmospheric albedo.

It should be noted that use of the average reflectivity and emissivity may cause extra accuracy loss. When the spectral reflectivity and emissivity are constants in spectral range from λ_1 to λ_2, the computational error will have a little effect on the results.

IV. EXAMPLES AND ANALYSIS

The developed model is suitable for the simulation of satellite images at a moderate spatial resolution. Radiance images are simulated in different MODIS bands to illustrate the usefulness of the proposed strategy. There is no specific reason to select the MODIS bands as examples except for the similar spatial resolution.

A. Earth Surface Scene

The MODIS images are simulated as an example for the observation of the Earth surface. The structural similarity (SSIM) [42], [52], [53] is used as a criteria to evaluate the simulation quantitatively, which is defined as

$$\mathrm{SSIM}(x, y) = \frac{(2\mu_x\mu_y + C_1)(2\sigma_{xy} + C_2)}{(\mu_x^2 + \mu_y^2 + C_1)(\sigma_x^2 + \sigma_y^2 + C_2)} \tag{23}$$

where μ_x and μ_y are the mean values of images x and y, respectively; σ_x and σ_y are their standard deviations; σ_{xy} is the covariance of x and y; and C_1 and C_2 are two defined constants

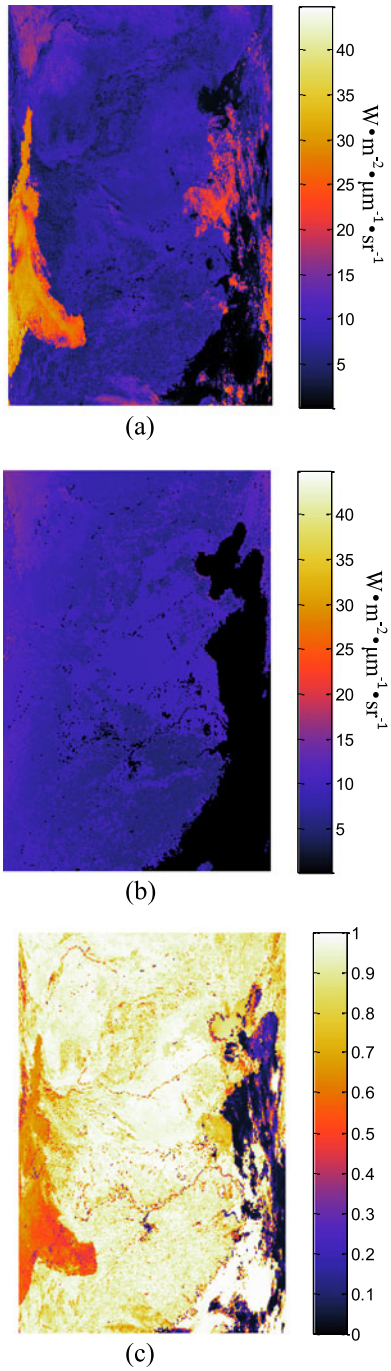

Fig. 4. Simulation of MODIS image in band 6 (1.628−1.652 μm). (a) MODIS image. (b) Calculated image. (c) SSIM image.

included to avoid unstable results when $\mu_x^2 + \mu_y^2$ and $\sigma_x^2 + \sigma_y^2$ are close to zero. In the simulation, C_1 and C_2 are set as 0.01 and 0.03, respectively, following the default value [53]. According to Wang *et al*. [53], the performance of the SSIM index is insensitive to the variations of these values.

A mean SSIM index (MSSIM) is used to evaluate the overall similarity of simulated images. Additionally, for the local similarity evaluation, an 11 × 11 circular-symmetric Gaussian weighting function moves pixel-by-pixel over the image to compute the local SSIM and generate a SSIM image. The MSSIM

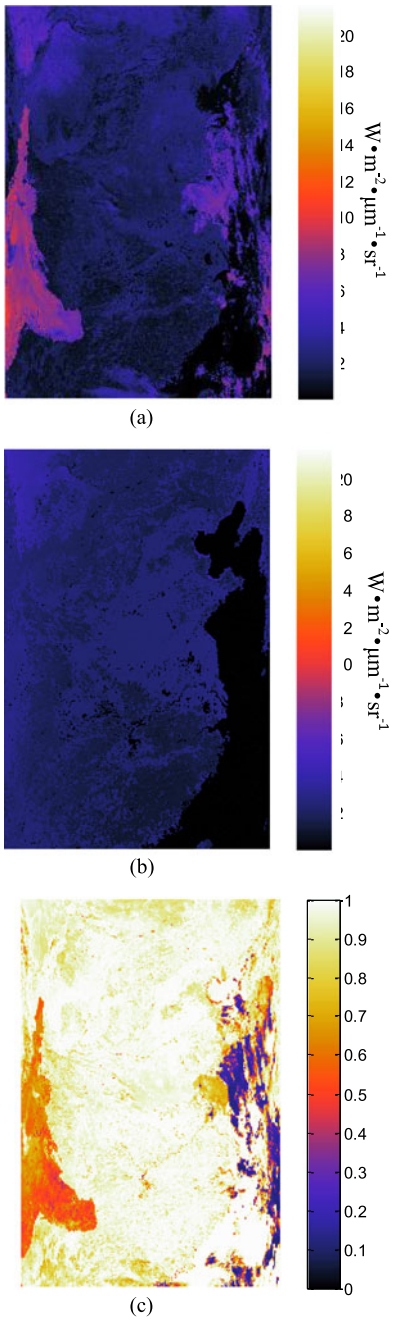

Fig. 5. Simulation of MODIS image in band 7 (2.105−2.155 μm). (a) MODIS image. (b) Calculated image. (c) SSIM image.

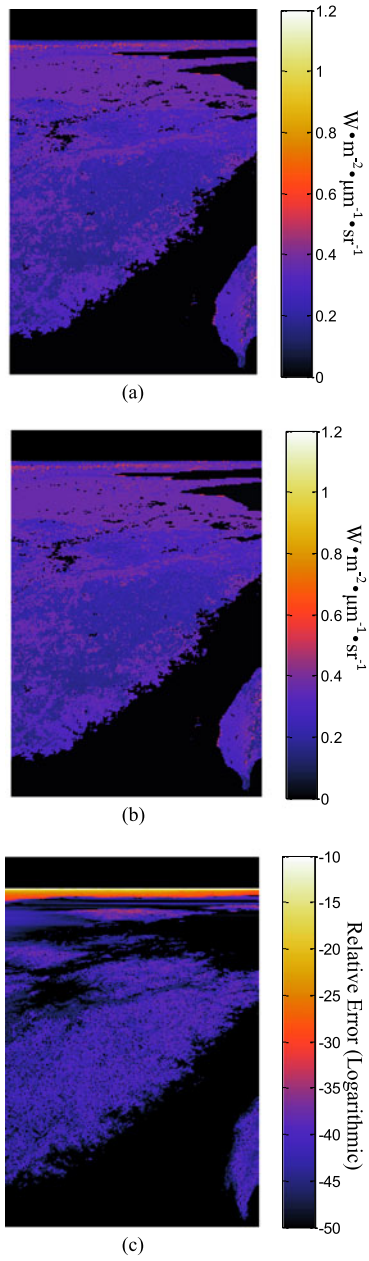

Fig. 6. Simulation of Earth limb scene in band 7 (2.105−2.155 μm). (a) Pixel-by-pixel calculation. (b) Proposed strategy. (c) Relative error image in logarithmic value.

index and the SSIM image are useful tools for the image quality assessment.

The files of the MODIS level 1 product can be downloaded from the NASA's website [54]. A scene of China eastern coast is selected to simulate images in band 6 (1.628−1.652 μm) and band 7 (2.105−2.155 μm). The simulation parameters are listed in Table II where the sensor parameters are given in [55].

The simulation results of the MODIS band 6 and band 7 are shown, respectively, in Figs. 4 and 5. Figs. 4(a) and 5(a) are the MODIS images in the unit of $\mathrm{W} \cdot \mathrm{m}^{-2} \cdot \mu\mathrm{m}^{-1} \cdot \mathrm{sr}^{-1}$. Figs. 4(b) and 5(b) are the simulated images with the same unit. Figs. 4(c) and 5(c) are the SSIM images. As it can be seen from Figs. 4 and 5, even though only one set of atmospheric conditions is used in the simulation, the SSIM values are higher than 0.9 in most cloudless areas since these two bands are insensitive to the aerosol conditions. However, the SSIM values of the cloudy areas are dramatically low since the reflectivity of cloud is more intense than surface. The MSSIM indices of band 6 and band 7 are, respectively, 0.818 and 0.887 when the SSIM values of the cloudy areas are included in statistics.

Even though the BOA images are generated with a database and a few semiempirical models, the physically based model allows simulating radiance images of the Earth surface with high similarities. A major drawback of the proposed strategy is that

TABLE III
SIMULATION PARAMETERS FOR ASSUMED SCENE SIMULATION

	Parameters	Value
Geometry	Greenwich Time (Starting)	2016.5.28, 8:28 a.m.
	Platform starting location	705.3 km, 115°E, 23°N
	Platform moving direction	East
	Nadir angle	−11.2° to 71.2°
Sensor	Number of detectors	2030
	Number of sampling points	1374
	IFOV	0.04°
	Radiometric accuracy	0.5%
	Spectral resolution	1 nm
	Bands	Band 7 (2.105−2.155 μm)
		Band 21 (3.929−3.989 μm)
		Band 25 (4.482−4.549 μm)
Specified Atmospheric Conditions	Atmospheric model	U.S. Standard 76
	Boundary aerosol type	Rural
	Relative humidity	0.99
	Visibility	18 km
LUTs	Solar zenith angles	54.9°−63.1° in step of 0.1°
	Viewing zenith angles	−12.2° to 90.0° in step of 0.2°
	Atmospheric layers	0−100 km, 60 layers in total

the spatial distributions of atmospheric conditions, especially for a swath covering large area, can hardly be obtained without using satellite images. For this reason, it is more appropriate to utilize the developed model to analyze the spectral characteristics of the Earth surface and atmosphere.

B. Earth Limb Scene

Due to the lack of available multispectral images for the Earth limb, a scene where the Earth limb can be observed is assumed to assess the performance of the proposed strategy for TOA radiance calculation. The results of the developed model are compared with pixel-by-pixel calculation in different spectral bands via relative error σ, which is defined as

$$\sigma = |L_{\mathrm{LUT}} - L_{\mathrm{PBP}}| / L_{\mathrm{PBP}} \tag{24}$$

where L_{LUT} is the radiance image calculated via the proposed strategy and L_{PBP} is the radiance image obtained from pixel-by-pixel calculation.

Three MODIS bands are subjectively selected as examples to illustrate spectral characteristic differences. Band 7 (2.105−2.155 μm), band 21 (3.929−3.989 μm), and band 25 (4.482−4.549 μm) represent the spectral bands with dominant scattering, emission, and absorption effects, respectively. Simulation parameters are listed in Table III.

To implement LUT interpolation, the spline interpolation function provided by the Matrix Laboratory (MATLAB) is used in the simulation. The results of bands 7, 21, and 25 are presented, respectively, from Figs. 6 through 8, where the images labeled with (a) are obtained from the pixel-pixel calculation; the images labeled with (b) are calculated via the proposed strategy; the images labeled with (c) are the relative error images of two approaches in logarithmic values.

The dominant radiance is surface reflection in band 7. As shown in Fig. 6, the reflection of the sea is less intense than the land. Due to topographic effect, a number of sparkling pixels are found in the radiance images which may lead to sensor saturation. The relative errors of two radiance images are less than 2×10^{-4} in most surface areas. However, when the line of sight direction approaches the horizon, the relative errors increase rapidly and peak at about 0.1 in the edge areas of the Earth surface. This phenomenon results from the rapid increase of scattered radiance at large zenith angles. The accuracy can be improved by setting more breakpoints in the LUTs at the cost of computational time. As a consequence, a compromise between accuracy and efficiency should be considered in building LUTs.

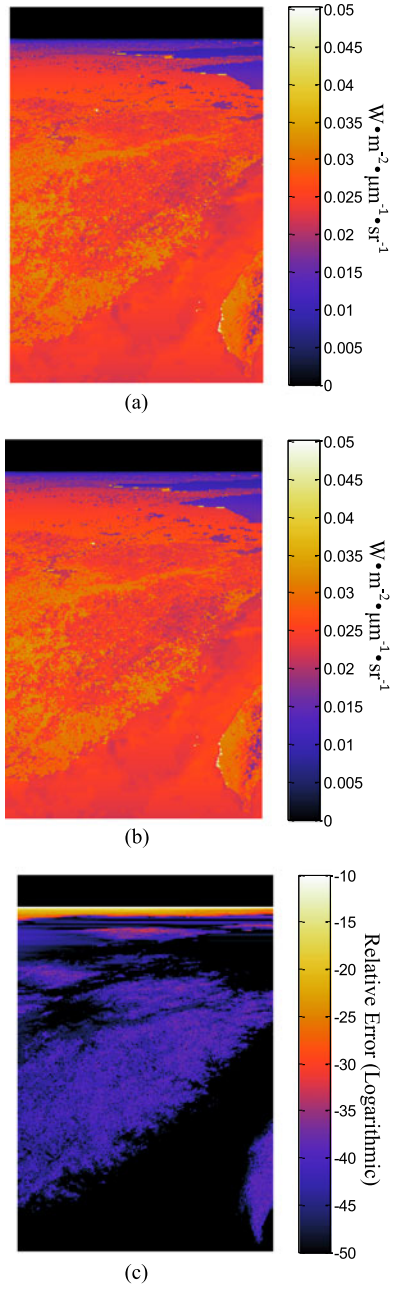

Fig. 7. Simulation of Earth limb scene in band 21 (3.929−3.989 μm). (a) Pixel-by-pixel calculation. (b) Proposed strategy. (c) Relative error image in logarithmic value.

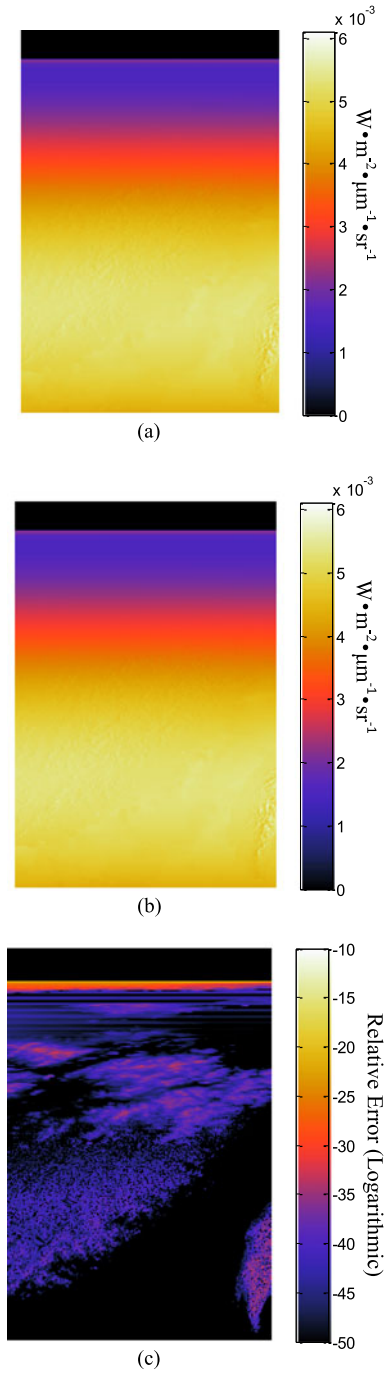

Fig. 8. Simulation of Earth limb scene in band 25 (4.482−4.549 μm). (a) Pixel-by-pixel calculation. (b) Proposed strategy. (c) Relative error image in logarithmic value.

The surface emission in band 21 is much more intense than that in band 7. As it can be seen from Fig. 7(a) and (b), the sea and the land are hard to be distinguished since their temperatures are almost the same. Comparing with radiance images in band 7, the radiant intense decrease dramatically at the edge area of the Earth surface due to the fact that the transmittance in band 21 is more sensitive to the variation of transfer path length. Additionally, although the emission effect is dominant, sparkling pixels with intense reflection are also observed in this band. In Fig. 7(c), the variation of relative error is similar to Fig. 6(c), i.e., the edge areas of the Earth surface have the maximum relative error.

Since the absorption effects are prominent in band 25, the texture of the Earth surface is hardly recognized in Fig. 8. Additionally, the Earth limb emission can be observed clearly as atmospheric emission is dominant in this band. Even though the variation of relative errors is almost unchanged, the maximum relative error in this band decreases remarkably to 9×10^{-3}. There is a reasonable explanation for this: since extinction coefficient is large in absorption spectral bands, atmospheric radiance is less sensitive to the variation of transfer path length as well as viewing zenith angle. As a result, the accuracy of LUT interpolation in band 25 is a little higher than that in bands 7 and 21.

TABLE IV
SIMULATION PARAMETERS FOR APPROXIMATION DIFFERENCE ANALYSIS

Parameters			Value
Atmospheric conditions	Real	Atmospheric model	Tropical
		Boundary aerosol type	Tropospheric
		Relative humidity	0.5
		Visibility	18 km
	Specified	Atmospheric model	Tropical
		Boundary aerosol type	Rural
		Relative humidity	0.9
		Visibility	5 km
Geometry		Solar zenith angle	40°
		Viewing zenith angle	20°
		Relative azimuth angle	100°
Surface		Altitude	0.5 km
		Assumed temperature	290 K
		Real temperature	313 K
		Type ID (IGBP)	1, 7, 13
LUTs		Atmospheric layers	0−100 km, 60 layers in total

C. Errors of Approximations

According to the discussions in Section III, two approximations are adopted in the developed model. One is proposed for various atmospheric conditions while the other is presented to avoid generating LUTs for each type of surface. Their performance will be analyzed in the following to find out suitable spectral ranges for application. The MODIS bands are chosen in accordance with the simulation in previous sections. The simulation parameters are given in Table IV.

Fig. 9 depicts the accuracy of the equivalent coefficient approximation for surface type 1 in spectrum spanning from 2 to 5 μm. The TOA spectral exitance is presented in Fig. 9(a) where the blue and the red profiles are calculated by the radiative transfer model and the approximation, respectively. The corresponding error and the relative error profiles are, respectively, shown in Fig. 9(b) and (c).

Since only the total transmittance is considered in the approximation with the equivalent coefficient, the relative errors of TOA exitance would be prominent in spectral bands with intense atmospheric scattered radiance. As it can be seen in Fig. 9,

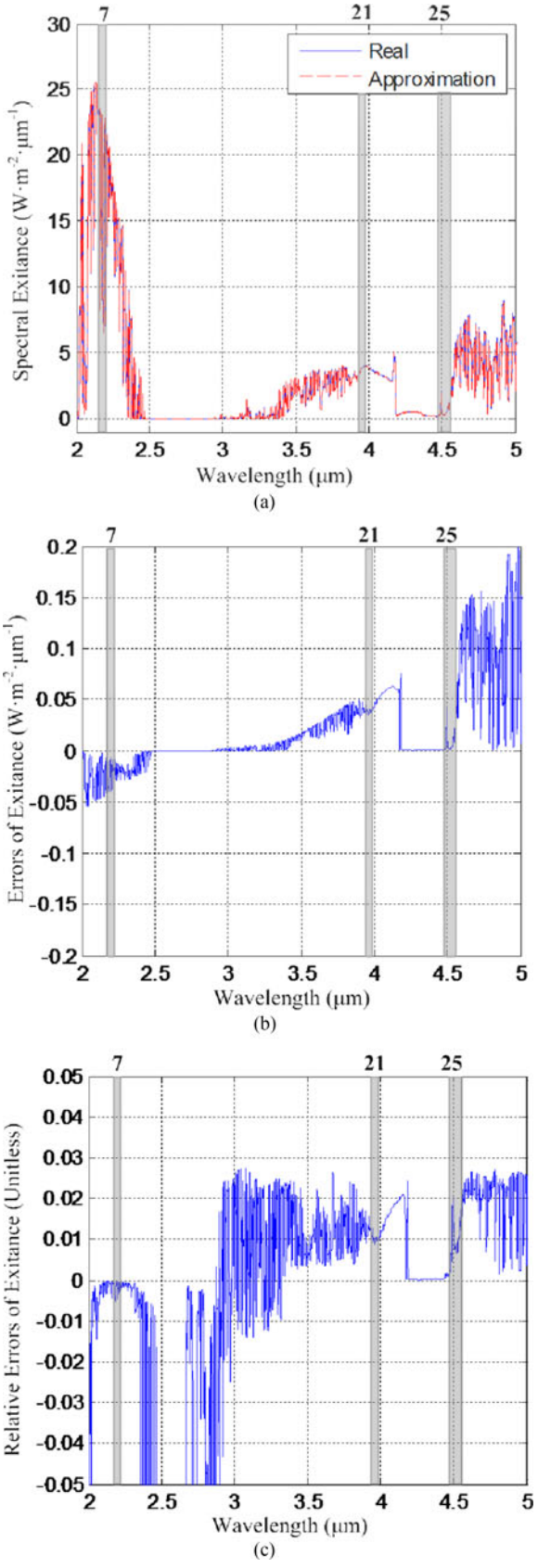

Fig. 9. Accuracy analysis of equivalent coefficient approximation for surface type 1 in spectrum spanning from 2 to 5 μm. (a) TOA spectral exitance in unit of $\mathrm{W{\cdot}m^{-2}{\cdot}\mu m^{-1}}$. (b) Error profile of TOA spectral exitance in unit of $\mathrm{W{\cdot}m^{-2}{\cdot}\mu m^{-1}}$. (c) Relative error profile of TOA spectral exitance.

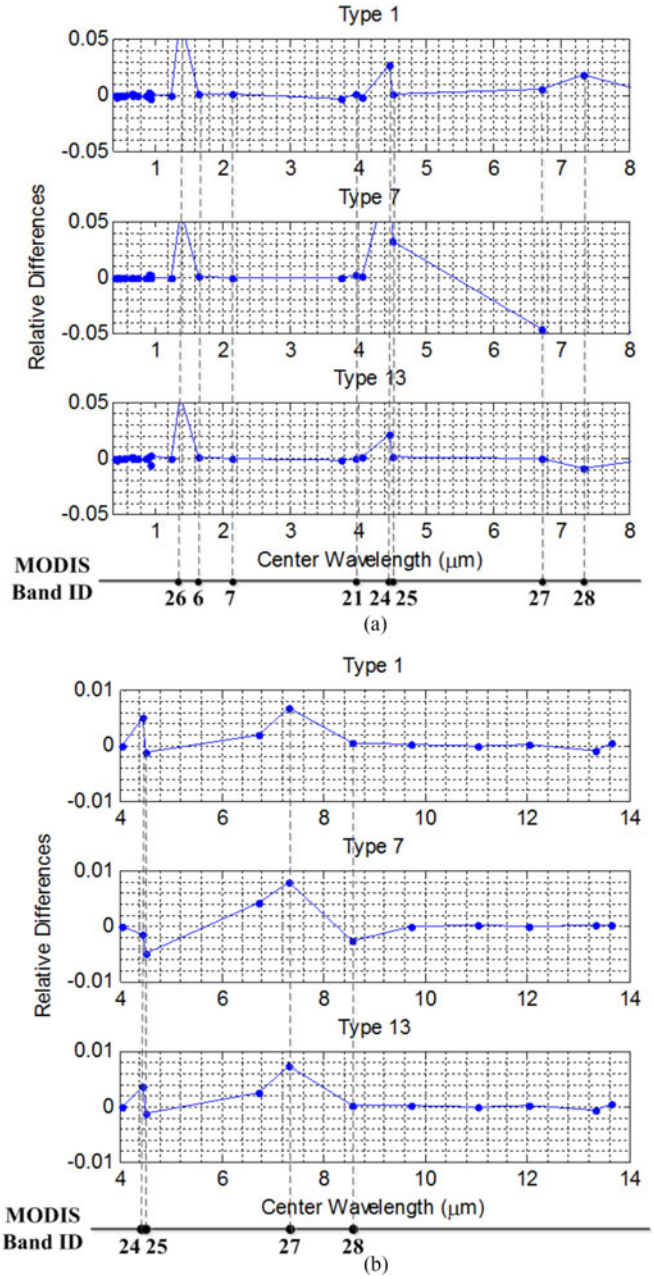

Fig. 10. Accuracy analysis of average reflectivity and emissivity approximation for surface type 1, 7, and 13. (a) Reflection. (b) Emission.

even though the errors of absorption bands, like 2.7 μm, are insignificant in Fig. 9(b), the relative errors of these bands are over 5.0×10^{-2} as shown in Fig. 9(c). The relative errors of other spectral bands are less than 3.0×10^{-2}, for instance, the relative errors for band 7, 21 and 25 are, respectively, -1.1×10^{-3}, 1.0×10^{-2}, and 1.2×10^{-3}.

According to previous descriptions, the accuracies of the average reflectivity and emissivity approximations are relate to atmospheric spectral transmittance. TOA spectral reflection and emission are calculated with the parameters in Table IV under the specified atmosphere conditions. The relative errors between the approximated results and the calculated TOA radiations are compared for different surface types. Fig. 10

shows the comparisons of surface types 1, 7, and 13. As it can be seen, the relative errors of the surface reflection and emission are significant for bands with intense absorption effects, such as band 26 (1.360−1.390 μm), band 24 (4.433−4.498 μm), band 25 (4.482−4.549 μm), band 27 (6.535−6.895 μm), and band 28 (7.175−7.475 μm). Except for these bands, the relative errors of the reflection and the emission in other bands are lower than 2×10^{-3}.

V. Conclusion

A physically based simulation model that allows multispectral image simulation from visible to thermal IR bands was developed for Earth observation sensors in this paper. In calculating TOA radiance image, a new strategy was proposed to improve accuracy as well as efficiency, where transmitted surface radiance and atmospheric radiance were calculated, respectively. The transmitted surface radiance image was obtained from pixel-by-pixel calculation of BOA radiance and path transmittance while two LUTs were built for efficient calculation of the emitted and the scattered atmospheric radiance. Two approximations were adopted to reduce necessary variables in building the LUTs, enabling more breakpoints without adding excessive computational burden.

Examples were presented to demonstrate the accuracy and the usefulness of the developed model. In the simulation of the Earth surface scene, the calculated images were compared with the MODIS data in bands 6 and 7 via SSIM. The SSIM indices in the cloudless areas were higher than 0.9 while the MSSIM were 0.81 and 0.88 in bands 6 and 7, respectively. The radiance images of an assumed scene where the Earth limb can be observed were simulated in different spectral bands to illustrate applicability of LUTs for scenes with extreme variable values. The simulated images were compared with the results of pixel-by-pixel calculation via relative errors in transmittance (bands 7 and 21) and absorption (band 25) bands. From the comparison, the relative errors were less than 2×10^{-4} in most surface areas for all these bands whereas the relative errors increased rapidly at the edge areas of the Earth surface. More breakpoints can be set in the LUTs to improve precision at the cost of computational time. Besides, to quantify the accuracy loss related to the approximations, the profiles of TOA spectral exitance calculated via approximations were compared with the results of radiative transfer model in spectrum spanning from 2 to 5 μm. The comparison indicated that the relative errors of the TOA spectral exitance were less than 3×10^{-2} in most MODIS bands. Additionally, although the relative errors of the spectral exitance were over 5×10^{-2} in bands with intense absorption effect like 2.7 μm, the absolute errors were small in these bands.

As shown in the experimental results, the developed model can be used to simulate multispectral images for scenes at moderate spatial resolution in various bands. Although errors were contained in the simulated images, the multispectral images characterize the physical features of the Earth surface and atmosphere. The developed model provides a validation platform for different algorithms, such as band selection and spectral classification.

References

[1] L. Guanterx *et al.*, "The EnMAP spaceborne imaging spectroscopy mission for earth observation," *Remote Sens.*, vol. 7, pp. 8830–8857, Jul. 2015.

[2] E. J. Hochberg, D. A. Roberts, P. E. Dennison, and G. C. Hulley, "Special issue on the hyperspectral infrared imager (HyspIRI): Emerging science in terrestrial and aquatic ecology, radiation balance and hazards," *Remote Sens. Environ.*, vol. 167, pp. 1–5, 2015.

[3] D. Drusch *et al.*, "Sentinel-2: ESA's optical high-resolution mission for GMES operational services," *Remote Sens. Environ.*, vol. 120, pp. 25–36, 2012.

[4] C. Donlon *et al.*, "The global monitoring for environment and security (GMES) sentinel-3 mission," *Remote Sens. Environ.*, vol. 120, pp. 37–57, 2012.

[5] S. Jia, Z. Ji, Y. Qian, and L. Shen, "Unsupervised band selection for hyperspectral imagery classification without manual band removal," *IEEE J. Sel. Topics Appl. Earth Observ. Remote Sens.*, vol. 5, no. 2, pp. 531–543, Apr. 2012.

[6] J. M. Bioucas-Dias *et al.*, "Hyperspectral unmixing overview: Geometrical, statistical, and sparse regression-based approaches," *IEEE J. Sel. Topics Appl. Earth Observ. Remote Sens.*, vol. 5, no. 2, pp. 354–379, Apr. 2012.

[7] S. Matteoli, M. Diani, and J. Theiler, "An overview of background modeling for detection of targets and anomalies in hyperspectral remotely sensed imagery," *IEEE J. Sel. Topics Appl. Earth Observ. Remote Sens.*, vol. 7, no. 6, pp. 2317–2336, Jun. 2014.

[8] Y. Chen, X. Zhao, and X. Jia, "Spectral-spatial classification of hyperspectral data based on deep belief network," *IEEE J. Sel. Topics Appl. Earth Observ. Remote Sens.*, vol. 8, no. 6, pp. 2381–2392, Jun. 2015.

[9] K. Segl *et al.*, "EeteS—The EnMAP end-to-end simulation tool," *IEEE J. Sel. Topics Appl. Earth Observ. Remote Sens.*, vol. 5, no. 2, pp. 522–530, Apr. 2012.

[10] K. Segl *et al.*, "S2eteS: An end-to-end modeling tool for the simulation of sentinel-2 image products," *IEEE Trans. Geosci. Remote Sens.*, vol. 53, no. 10, pp. 5560–5571, Oct. 2015.

[11] W. Verhoef and H. Bach, "Simulation of sentinel-3 images by four-stream surface-atmosphere radiative transfer modeling in the optical and thermal domains," *Remote Sens. Environ.*, vol. 120, pp. 197–207, 2012.

[12] A. Borner *et al.*, "SENSOR: A tool for the simulation of hyperspectral remote sensing systems," *ISPRS J. Photogramm. Remote Sens.*, vol. 55, no. 5-6, pp. 299–312, 2001.

[13] M. E. Schaepman *et al.*, "Advanced radiometry measurements and earth science applications with the airborne prism experiment (APEX)," *Remote Sens. Environ.*, vol. 158, pp. 207–219, 2015.

[14] W. Verhoef and H. Bach, "Simulation of hyperspectral and directional radiance images using coupled biophysical and atmospheric radiative transfer models," *Remote Sens. Environ.*, vol. 87, pp. 23–41, 2003.

[15] J. Vicent *et al.*, "FLEX end-to-end mission performance simulator," *IEEE Trans. Geosci. Remote Sens.*, vol. 54, no. 7, pp. 4215–4222, Nov. 2016.

[16] M. Parente, J. T. Clark, A. J. Brown, and J. L. Bishop, "End-to-end simulation and analytical model of remote-sensing systems: Application to CRISM," *IEEE Trans. Geosci. Remote Sens.*, vol. 48, no. 11, pp. 3877–3888, Nov. 2010.

[17] J. R. Schott, S. D. Brown, R. V. Raqueno, H. N. Gross, and G. Robinson, "An advanced synthetic image generation model and its application to multi/hyperspectral algorithm development," *Can. J. Remote Sens.*, vol. 25, no. 2, pp. 99–111, Jun. 1999.

[18] S. A. Cota *et al.*, "PICASSO: An end-to-end image simulation tool for space and airborne imaging systems," *J. Appl. Remote Sens.*, vol. 4, pp. 1–36, Jun. 2010.

[19] J. P. Gastellu-Etchegorry, E. Martin, and F. Gascon, "DART: A 3-D model for simulating satellite images and studying surface radiation budget," *Int. J. Remote Sens.*, vol. 25, no. 1, pp. 73–96, Jan. 2004.

[20] Y. Liu, W. Zhang, and B. Zhang, "Top-of-atmosphere image simulation in the 4.3-μm mid-infrared absorption bands," *IEEE Trans. Geosci. Remote Sens.*, vol. 54, no. 1, pp. 452–465, Jan. 2016.

[21] Y. Zhang, X. Yu, G. Wang, and X. Zhou, "Independent component analysis based band selection of multispectral remote sensing image," in *Proc. IEEE Int. Symp. Geosci. Remote Sens.*, 2014, vol. 1, pp. 517–520.

[22] T. Veracini, S. Matteoli, M. Diani, and G. Corsini, "Robust hyperspectral image segmentation based on a non-Gaussian model," in *Proc. 2010 2nd Int. Workshop Cogn. Inf. Process.*, 2010, vol. 1, pp. 192–197.

[23] H. E. M. Viggh and D. H. Staelin, "Spatial surface prior information reflectance estimation (SPIRE) algorithms," *IEEE Trans. Geosci. Remote Sens.*, vol. 41, no. 11, pp. 2424–2435, Nov. 2003.

[24] S. W. Wharton, "A spectral-knowledge-based approach for urban land-cover discrimination," *IEEE Trans. Geosci. Remote Sens.*, vol. GE-25, no. 3, pp. 272–282, May 1987.
[25] J. Settle, "On constrained energy minimization and the partial unmixing of multispectral images," *IEEE Trans. Geosci. Remote Sens.*, vol. 40, no. 3, pp. 718–712, Mar. 2002.
[26] L. Guanter, R. Richter, and H. Kaufmann, "On the application of the MODTRAN4 atmospheric radiative transfer code to optical remote sensing," *Int. J. Remote Sens.*, vol. 30, no. 6, pp. 1407–1424, Mar. 2009.
[27] L. Guanter, K. Segl, and H. Kaufmann, "Simulation of optical remote-sensing scenes with application to the EnMAP hyperspectral mission," *IEEE Trans. Geosci. Remote Sens.*, vol. 47, no. 7, pp. 2340–2351, Jul. 2009.
[28] X. He and X. Xu, "Fast calculation of scattered radiance in multispectral imagery simulation," in *Proc. SPIE, Infrared Remote Sens. Instrum. XXIII*, 2015, vol. 9608, no. 96080O, pp. 1–11.
[29] U. S. Geological Survey (USGS). (2012, Feb.). Global Land Cover Characterization Data Base Version 2.0. [Online]. Available: http://edc2.usgs.gov/glcc/globdoc2_0.php
[30] D. E. Bowker, R. E. Davis, D. L. Myrick, K. Stacy, and W. T. Jones, *Spectral Reflectances of Natural Targets for Use in Remote Sensing Studies*. Washington, DC, USA: NASA, Ref. Publication RP-1139, Jun. 1985.
[31] R. N. Clark *et al.* (2007, Sep.). USGS Digital Spectral Library splib06a: U.S. Geological Survey, Digital Data Series 231. USGS, Reston, VA. [Online]. Available: http://speclab.cr.usgs.gov/spectral.lib06
[32] Z. Wan. (1999, Nov.). MODIS UCSB Emissivity Library. Inst. for Comput. Earth Syst. Sci. [Online]. Available: http://www.icess.ucsb.edu/modis/EMIS/html/em.html
[33] C. Amante and B. W. Eakins, "ETOPO1 1 arc-minute global relief model: Procedures, data source and analysis," NOAA, Boulder, CO, USA, Tech. Memorandum NESDIS NGDC-24, Mar. 2009.
[34] R. J. Hijmans, S .E. Cameron, J. L. Parra, P. G. Jones, and A. Jarvis, "Very high resolution interpolated climate surfaces for global land areas," *Int. J. Climatol.*, vol. 25, pp. 1965–1978, Sep. 2005.
[35] G. Feldman and N. Kuring. (2014). Sea Surface Temperature (1 Month – AQUA/MODIS). NASA Ocean Color Group, Washington, DC, USA. [Online]. Available: http://neo.sci.gsfc.nasa.gov/view.php?datasetId=MYD28M
[36] R. Muller and E. Muller (2012, Dec.). Berkeley Earth Surface Temperature. Berkeley Earth, Berkeley, CA. [Online]. Available: http://berkeleyearth.org/source-files/
[37] C. O. Justice *et al.*, "The moderate resolution imaging spectroradiometer (MODIS): Land remote sensing for global change research," *IEEE Trans. Geosci. Remote Sens*, vol. 36, no. 4, pp. 1228–1249, Jul. 1998.
[38] C. Cao, F. J. De Luccia, X. Xiong, R. Wolfe, and F. Weng, "Early on-orbit performance of the visible infrared imaging radiometer suite onboard the suomi national polar-orbiting partnership (S-NPP) satellite," *IEEE Trans. Geosci. Remote Sens*, vol. 52, no. 2, pp. 1142–1156, Feb. 2014.
[39] X. Shi and X. Xu, "Impact of background radiation on the detection performance of interceptor seekers," *Syst. Eng. Electron.*, vol. 32, no. 10, pp. 2053–2056, Oct. 2010.
[40] B. J. Cooke *et al.*, "Modeling the MTI electro-optic system sensitivity and resolution," *IEEE Trans. Geosci. Remote Sens.*, vol. 43, no. 9, pp. 1950–1962, Sep. 2005.
[41] H. Rahman, B. Pinty, and M. M. Verstraete, "Coupled surface atmosphere reflectance (CSAR) model 2. Semiempirical surface model usable with NOAA advanced very high resolution radiometer data," *J. Geophys. Res.*, vol. 98, no. D11, pp. 20791–20801, Nov. 1993.
[42] I. Sola, M. G. Audicana, J. A. Mozos, and J. L. Torres, "Synthetic images for evaluating topographic correction algorithms," *IEEE Trans. Geosci. Remote Sens*, vol. 52, no. 3, pp. 1799–1810, Mar. 2014.
[43] J. Wen, Q. Liu, Q. Liu, Q. Xiao, and X. Li, "Parametrized BRDF for atmospheric and topographic correction and albedo estimation in Jiangxi rugged terrain, China," *Int. J. Remote Sens.*, vol. 30, no. 11, pp. 2875–2896, Jun. 2009.
[44] G. S. Johnson, J. Lee, C. A. Burns, and W. R. Mark, "The irregular Z-buffer: Hardware acceleration for irregular data structures," *ACM Trans. Graph.*, vol. 24, no. 4, pp. 1462–1482, Oct. 2005.
[45] T. R. Loveland *et al.*, "Development of a global land cover characteristics database and IGBP DISCover from 1 km AVHRR data," *Int. J. Remote Sens.*, vol. 21, no. 6 and 7, pp. 1303–1330, 2000.
[46] A. C. Wilber, D. P. Kratz, and S. K. Gupta, "Surface emissivity maps for use in satellite retrievals of longwave radiation," NASA, Hampton, VA, USA, NASA/TP-1999-209362, Aug. 1999.
[47] W. M. Cornette, J. M. Alfred, and J. M. Goldspiel, *Moderate Spectral Atmospheric Radiance and Transmittance (MOSART) Code Technical Reference Manual Part 2: Terrain, Hydrometeors, Electrical Discharge Phenomena, Oceans, and Space*, NRL, Washington, DC, USA, Tech. Ref. Man. MOSART-NRL-DOC-TRM-001-1103031, Mar. 2011.
[48] A. Berk, L. S. Bernstein, and D. C. Robertson, "MODTRAN: A moderate resolution model for LOWTRAN7," AFGL, Burlington, MA, USA, Tech. Rep. AFGL-TR-89-0122, Jul. 08, 1987.
[49] E. F. Vermote, D. Tanre, L. Deuze, M. Herman, and J. Morcrette, "Second simulation of the satellite signal in the solar spectrum, 6S: An overview," *IEEE Trans. Geosci. Remote Sens*, vol. 35, no. 3, pp. 675–686, May 1997.
[50] P. Ricchiazzi, S. Yang, C. Gautier, and D. Sowle, "SBDART: A research and teaching software tool for plane parallel radiative transfer in the earth's atmosphere," *Bull. Amer. Meteorol. Soc.*, vol. 79, no. 10, pp. 2010–2114, May 1998.
[51] E. P. Shettle and R. W. Fenn, "Models for the aerosols of the lower atmosphere and the effects of humidity variations on their optical properties," AFGL, Hanscom AFB, MA, USA, Tech. Rep. AFGL-TR-79-0214, Sep. 20, 1979.
[52] D. Brunet, E. R. Vrscay, and Z. Wang, "On the mathematical properties of the structural similarity index," *IEEE Trans. Image Process.*, vol. 21, no. 4, pp. 1488–1499, Apr. 2012.
[53] Z. Wang, A. C. Bovik, H. R. Sheikh, and E. P. Simoncelli, "Image quality assessment: From error visibility to structural similarity," *IEEE Trans. Image Process.*, vol. 13, no. 4, pp. 600–606, Apr. 2004.
[54] G. N. Toller, A. Isaacman, J. Kuyper, and X. Geng. (2012, Jul.). MODIS level 1B Product User's Guide for Level 1B Version 6.1.14 (Terra) and Version 6.1.17 (Aqua). NASA, Greenbelt, MD, MCST Document, PUB-01-U-0202-REV D. [Online]. Available: http://ladsweb.nascom.nasa.gov
[55] T. S. Pagano and R. M. Durhan, "Moderate resolution imaging spectroradiometer (MODIS)," in *Proc. SPIE, Sensor Syst. Early Earth Observing Syst. Platforms*, 1993, vol. 1939, pp. 2–17.

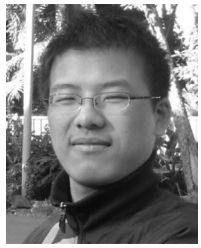

Xiaoyu He was born in Jiangxi, China, in 1991. He received the B.S. degree from the School of Mechanical and Electric Engineering, Guangzhou University, Guangzhou, China, in 2012. He is currently working toward the Ph.D. degree in signal and information processing in the School of Electronics and Information Engineering, Beihang University, Beijing, China.

His current research interests include understand and calculation of infrared radiative prorogation in the atmosphere.

Xiaojian Xu was born in Jiangxi, China, in 1963. He received the B.S. degree from the Hefei University of Technology, Hefei, China, in 1983, the M.S. degree from the Beijing Institute of Environmental Features (BIEF), Beijing, China, in 1986, and the Ph.D. degree from the University of Nebraska, Lincoln, NE, USA, in 2002, all in electrical engineering.

He was with BIEF from 1986 to 1999, where he was mainly involved in research of electromagnetic scattering modeling and microwave imaging. From June 1999 to December 2002, he was with the Environmental Remote Sensing Laboratory, University of Nebraska, where he was involved in the research work on ultrawideband random noise radar, with emphasis on foliage and ground-penetration applications. Since January 2003, he has been with the School of Electronics and Information Engineering, Beihang University, Beijing, as a Signal and Information Processing Professor. His current research interests include remote sensing signatures, radar imagery, target recognition, and system modeling.